



## Velocity asymmetry and turbulent transport closure in smooth- and rough-wall boundary layers

Michael Heisel <sup>1,2,3,\*</sup> Gabriel G. Katul,<sup>4,5</sup> Marcelo Chamecki <sup>1</sup> and Michele Guala<sup>2,3</sup>

<sup>1</sup>*Department of Atmospheric & Oceanic Sciences, University of California in Los Angeles, Los Angeles, California, USA*

<sup>2</sup>*St. Anthony Falls Laboratory, University of Minnesota, Minneapolis, Minnesota, USA*

<sup>3</sup>*Department of Civil, Environmental, and Geo- Engineering, University of Minnesota, Minneapolis, Minnesota, USA*

<sup>4</sup>*Nicholas School of the Environment, Duke University, Durham, North Carolina, USA*

<sup>5</sup>*Department of Civil and Environmental Engineering, Duke University, Durham, North Carolina, USA*



(Received 29 June 2020; accepted 23 September 2020; published 14 October 2020)

Sweep and ejection events in turbulent boundary layer flows have been explored for half a century now to describe eddies impacting turbulent stresses. Yet, moving these studies from their current diagnostic phase to a prognostic form remains a formidable challenge. Here, a cumulant expansion is used to derive a link between the transport of shear stress and the balance of local sweep and ejection events. Cumulant expansion is further used to connect this transport to a metric of asymmetry in the streamwise velocity distribution. These relations are employed to develop two so-called structural models for predicting the turbulent stress transport, which is traditionally neglected in first-order closure of the shear stress budget. Several datasets collected in rough-wall conditions are used to show the importance of the transport term in the roughness sublayer and to demonstrate the predictive skill of the two structural models. The model parameters are invariant to the tested range of Reynolds number and surface roughness, indicating the structural similarity between the velocity asymmetry, sweep/ejection balance, and stress transport may be universal and independent of roughness. Finally, the implementation of the structural models for improved closure schemes of the shear stress budget in modeling applications and wall-modeling in large-eddy simulations are discussed.

DOI: [10.1103/PhysRevFluids.5.104605](https://doi.org/10.1103/PhysRevFluids.5.104605)

### I. INTRODUCTION

In turbulent boundary layers, the turbulent motions transporting momentum [1] are classified as one of two types of events: “ejections” and “sweeps” [2]. These events are commonly detected by conditional sampling using quadrant analysis, which partitions the instantaneous turbulent momentum flux into ejections, sweeps, inward interactions, and outward interactions [3–7]. Ejection/sweep statistics along with their contribution to the time-averaged turbulent momentum flux have been extensively measured for a multitude of flow conditions: canonical smooth- and rough-wall boundary layers [8–11]; stratified atmospheric flows over vegetated surfaces [12,13] and complex terrain covered by vegetation [14–16]; various canopy covers [17–26] including peatlands [27], urban roughness sublayers [28,29], and street canyons [30]; convective boundary layers [31–33]; marine boundary layers [34]; air-water exchanges [35]; and even flow below ice sheets [36], to list a few

---

\*heisel@ucla.edu

examples. A review of the history, development, usage, and extensions of quadrant analysis and conditional sampling in turbulence is presented elsewhere [7,37].

Such quadrant analyses revealed that sweep events contribute more than ejections to the overall turbulent shear stress in the buffer region of smooth-wall turbulent boundary layers [3,8]. Specifically, the contribution of sweeps is greater for  $z^+ = zu_\tau/\nu \gtrsim 15$ , where  $z$  is the wall-normal distance from the surface,  $u_\tau$  is the friction velocity,  $\nu$  is the kinematic viscosity, and the transition point  $z^+ = 15$  is also the location of the turbulence intensity peak [38]. Likewise, analyses of rough-wall flows demonstrated unequivocally that sweeps are the primary contributor to the shear stress close to rough surfaces (including vegetation cover), and that the relative contribution of the sweep events increases both with increased surface roughness and with proximity to the surface [9,11,39–41]. In analogy to the smooth-wall buffer region, a number of studies have proposed that the extent of the roughness sublayer (hereafter referred to as the RSL) [9] as well as the canopy sublayer (hereafter the CSL) [15,21] are closely related to the region where sweep events are statistically more significant than ejections in their contribution to the shear stress. Within the RSL and CSL, flow statistics are directly dependent on the surface roughness or canopy properties.

Moving above the buffer region, RSL, or CSL, the contributions of sweep and ejection events to the turbulent shear stress are approximately equal in the overlap or logarithmic (log) region where the turbulent shear stress is constant [42]. In the outermost wake region of turbulent boundary layers, ejection events dominate the transport of momentum [3,8,9]. While this emerging picture has elucidated some aspects of the role of surface roughness and coherent motions in the transport of momentum, it has not been exploited effectively in conventional turbulence modeling or wall modeling in large-eddy simulations. Establishing links between quadrant analysis and Reynolds-averaged turbulence modeling has been, to say the least, fraught with challenges that partly motivate the present work.

A promising way forward from quadrant analysis is to model the probability density function (pdf) of flow variables using a cumulant expansion method (CEM) such as Gram-Charlier expansions [5,43,44]. Gram-Charlier expansions represent the pdf as a Gaussian distribution shaped with a series of adjustments arising from higher-order cumulants. For instance, the third-order cumulant accounts for the distribution asymmetry in terms of the skewness and the fourth-order cumulant accounts for the intermittency or flatness in terms of the excess kurtosis. The CEM can be extended to additional dimensions to model joint probability density functions (jpdfs) of two or more variables. Previous efforts used cumulant expansions of jpdfs to link the contributions of sweep and ejection events to budget equations of turbulent statistics [8,9]. To illustrate, the turbulent kinetic energy (TKE) budget equation for stationary and planar homogeneous conditions is considered. This budget is given by

$$\frac{\partial \bar{e}}{\partial t} = 0 = -\overline{u'w'} \frac{\partial U}{\partial z} - \frac{\partial}{\partial z} [F_{\text{TKE}} + \overline{p'w'}] - \epsilon, \quad (1)$$

where  $t$  is time,  $e = \frac{1}{2}(u'^2 + v'^2 + w'^2)$  is the instantaneous TKE,  $u'$ ,  $v'$ , and  $w'$  are the turbulent velocity components in the streamwise ( $x$ ), spanwise ( $y$ ), and wall-normal ( $z$ ) directions, respectively,  $p'$  is the turbulent pressure, primed quantities are fluctuations around the time-averaged state,  $\epsilon$  is the TKE dissipation rate,  $U$  is the mean velocity, and  $F_{\text{TKE}} = \frac{1}{2}(\overline{u'^2 w'} + \overline{v'^2 w'} + \overline{w'^3})$  is the wall-normal transport of TKE by turbulence. In addition to the pressure and dissipation terms,  $F_{\text{TKE}}$  requires a closure model in a second-order closure framework. Using a CEM to model the velocity probabilities in terms of third-order cumulants [5], Raupach [9] related the TKE transport to sweeping and ejecting motions as

$$F_{\text{TKE}} = a_1 \Delta S_o (a_2 \sigma_u^2 \sigma_w + a_3 \sigma_w^3), \quad (2)$$

where  $\Delta S_o \in [-1, 1]$  signifies the relative fractional contributions of ejections and sweeps to the turbulent momentum flux  $\overline{u'w'}$ ,  $\sigma_i$  is the root-mean square (rms) of the specified velocity component, and  $a_{1,2,3}$  are constants determined from experiments.

The value of the fractional stress contribution  $\Delta S_o$  indicates whether sweeps are favored ( $\Delta S_o > 0$ ), ejections are favored ( $\Delta S_o < 0$ ), or the two are balanced ( $\Delta S_o \approx 0$ ). The balance of ejections and sweeps therefore determines the sign of  $F_{\text{TKE}}$  in Eq. (2) and dictates whether turbulent kinetic energy at a given wall-normal position is transported to or from the surface. The influence of ejections and sweeps on net transport is a consideration that cannot be ignored in studies of the TKE budget [8], especially in the RSL and CSL. In fact, the increasingly dominant role of sweeps in the RSL with increasing roughness has already been pointed out by the pioneering work of Nakagawa and Nezu [8], but translating this result to wall modeling has remained elusive.

Equation (2) also deviates from classical gradient-diffusion schemes conventionally used to close third-order statistics through gradients in second-order moments [45]. Such gradient-diffusion closure of third-order statistics ( $F_{\text{TKE}} \propto \partial \bar{e} / \partial z$ ) remain the cornerstone of many operational atmospheric mesoscale models such as the Weather Research and Forecasting Model (WRF) [46] despite well-known limitations within the canopy sublayer [22,47]. Eq. (2) has been referred to as a “structural model” for  $F_{\text{TKE}}$  as discussed elsewhere [48]. In essence, structural models assume that the structure of turbulent eddies dominating ejections and sweeps are similar in all wall-bounded flows (i.e., a form of structural similarity where  $a_{1,2,3}$  do not vary with roughness).

While ejection/sweep statistics and their contribution to the TKE budget have been closely studied [8,9], their role in the momentum flux budget and corresponding closure model approximations have not been considered to the same degree, which is the compass of the work here. Note that the terminology momentum flux and turbulent shear stress are used interchangeably in this study to describe the covariance term  $\overline{u'w'}$ . In classical gradient diffusion closure for the turbulent shear stress (referred to as K-theory),

$$\overline{u'w'} = -K_T \frac{\partial U}{\partial z}, \quad (3)$$

where  $K_T$  is the eddy diffusivity. A large corpus of experiments and theories support (3) in the log region but K-theory is known to be insufficient in the RSL and CSL [22,49–52].

The present study uses cumulant expansions to seek a connection between the deviations from gradient diffusion closure in Eq. (3), the turbulent transport term in the shear stress budget (analogous to  $F_{\text{TKE}}$ ), and the imbalance in the contributions of ejections and sweeps to  $\overline{u'w'}$ . An outcome of this approach is a “structural” closure model to estimate the transport term that is traditionally neglected in gradient-diffusion methods. A variant on the proposed structural model is then formulated based on a simpler measure of asymmetry in the streamwise velocity, thereby bridging the imbalance of ejection and sweep motions to the basic shape of the velocity probability distributions. The purpose of the two models is to circumvent the failures of gradient-diffusion methods by providing an additional closure based on CEM to account for the transport term, which is particularly relevant in the RSL and CSL. The general applicability of these two formulations of the structural model is then analyzed using wind tunnel measurements and a publicly available direct numerical simulation (DNS). Whether third-order CEM applies in such flows and to what extent the structural model parameters (analogous to  $a_{1,2,3}$  in  $F_{\text{TKE}}$ ) are independent of surface roughness is discussed.

## II. THEORY

### A. Definitions and general considerations

In a neutrally stratified stationary and planar-homogeneous flow, the budget for the turbulent momentum flux  $\overline{u'w'}$  is

$$\frac{\partial \overline{u'w'}}{\partial t} = 0 = -\overline{w'w'} \frac{\partial U}{\partial z} - \frac{\partial \overline{u'w'w'}}{\partial z} + \overline{p' \left( \frac{\partial u'}{\partial z} + \frac{\partial w'}{\partial x} \right)} - \epsilon_{uw}, \quad (4)$$

where  $\epsilon_{uw}$  is molecular destruction of  $\overline{u'w'}$ . The terms on the right-hand side of Eq. (4) are, respectively, covariance production by the mean velocity gradient, vertical gradient of the turbulent

flux transport term (to be analyzed here), pressure-velocity decorrelation, and decorrelation by viscous effects. The viscous decorrelation  $\epsilon_{uw}$  can be ignored at high Reynolds numbers when compared to the pressure-velocity decorrelation [50].

A linear Rotta model, revised to include isotropization of the production term [45,53], is now used to close the pressure decorrelation term and is given as

$$p' \left( \frac{\partial u'}{\partial z} + \frac{\partial w'}{\partial x} \right) = -C_R \frac{\overline{u'w'}}{\tau} + C_I \overline{w'w'} \frac{\partial U}{\partial z}, \quad (5)$$

where  $C_R$  is the Rotta constant and  $C_I$  is the isotropization of the production constant predicted from rapid distortion theory to be  $\frac{3}{5}$  [53]. The closure in Eq. (5), in combination with Eq. (4), yields an expression for  $\overline{u'w'}$  given by

$$\overline{u'w'} = -\frac{\tau}{C_R} \left[ (1 - C_I) \sigma_w^2 \frac{\partial U}{\partial z} + \frac{\partial \overline{u'w'w'}}{\partial z} \right], \quad (6)$$

where  $\tau = \bar{e}/\epsilon$  is a relaxation timescale estimating the time it takes for  $u'$  to decorrelate from  $w'$ . K-theory in Eq. (3) is now recovered when the flux-transport term  $\partial \overline{u'w'w'}/\partial z$  is neglected relative to the production term, resulting in an eddy diffusivity  $K_T = [(1 - C_I)/C_R] \sigma_w^2 \tau$ . This finding resembles predictions of  $K_T$  from Lagrangian structure function analysis that yield  $K_T = 2\sigma_w^2 T_L$ , where  $T_L$  is the Lagrangian timescale as discussed elsewhere [53]. That is,  $K_T$  scales with  $\sigma_w$  ( $\sigma_w T_L$ ) or  $\sigma_w$  ( $\sigma_w \tau$ ) as characteristic velocity and length scales instead of the mixing length closure  $K_T = [\ell_m (\partial U / \partial z)] \ell_m$  [54], where  $\ell_m$  is a generic mixing length proportional to  $z$  in the logarithmic region of boundary layers [55,56]. The connection between sweeps and ejections and  $\overline{u'w'w'}$ , which is the ‘‘parent term’’ responsible for the failure of gradient-diffusion theory across many flows [57,58], is now considered using Gram-Charlier expansion and structural models.

## B. Structural models for the turbulent momentum flux transport term

### 1. Model 1: Fractional stress contributions

As noted earlier, a measure to characterize the relative importance of ejections and sweeps (i.e.,  $\Delta S_o$ ) on momentum fluxes is defined as [9]

$$\Delta S_o = \frac{\langle u'w' \rangle|_4 - \langle u'w' \rangle|_2}{\overline{u'w'}}, \quad (7)$$

where  $\langle u'w' \rangle|_i$  is a conditional average of events in quadrant  $i$ , with quadrant 2 corresponding to ejections ( $u' < 0, w' > 0$ ) and quadrant 4 to sweeps ( $u' > 0, w' < 0$ ). Explicitly,  $\Delta S_o$  quantifies the fractional difference between the contributions of ejection and sweep events to the overall time-averaged flux  $\overline{u'w'}$ , where the sign indicates whether sweeps ( $\Delta S_o > 0$ ) or ejections ( $\Delta S_o < 0$ ) are favored. No threshold on the instantaneous values of  $u'w'$  is used to compute  $\Delta S_o$ , and hence the subscript ‘‘o’’ is given to  $\Delta S$ . Raupach [9] used a third-order CEM of the joint probability jpdf( $u', w'$ ) to link  $\Delta S_o$  with the key statistical moments to be employed in closure modeling of the flow:

$$\Delta S_o = \frac{M_{11} + 1}{M_{11} \sqrt{2\pi}} \left[ \frac{2C_1}{(1 + M_{11})^2} + \frac{C_2}{1 + M_{11}} \right], \quad (8)$$

where  $C_1$  and  $C_2$  are given by

$$\begin{aligned} C_1 &= (1 + M_{11}) \left[ \frac{1}{6} (M_{03} - M_{30}) + \frac{1}{2} (M_{21} - M_{12}) \right] \\ C_2 &= - \left[ \frac{1}{6} (2 - M_{11}) (M_{03} - M_{30}) + \frac{1}{2} (M_{21} - M_{12}) \right], \end{aligned} \quad (9)$$

and the notation  $M_{ij}$  is used here to describe different statistical (mixed) moments of  $u'$  and  $w'$  as

$$M_{ij} = \frac{\overline{u'^i w'^j}}{\sigma_u^i \sigma_w^j}. \quad (10)$$

That is,  $M_{11}$  defines the correlation coefficient  $\overline{u'w'}/(\sigma_u\sigma_w)$ ,  $M_{30}$  and  $M_{03}$  define individual skewnesses of  $u'$  and  $w'$ , respectively, and  $M_{12}$  (associated with wall-normal turbulent transport of flux) and  $M_{21}$  (associated with wall-normal turbulent transport of longitudinal velocity variance) define third-order mixed moments. By substituting the constants in Eq. (9) into the CEM in Eq. (8) and rearranging the terms, the final form is reached for the CEM linking  $\Delta S_o$  to the statistical moments:

$$\Delta S_o = \frac{1}{M_{11}2\sqrt{2\pi}} \left[ \frac{M_{11}}{3}(M_{03} - M_{30}) + (M_{21} - M_{12}) \right]. \quad (11)$$

In Eq. (11) the mixed moments ( $M_{21} - M_{12}$ ) have been shown to contribute more to  $\Delta S_o$  than the skewnesses  $\frac{1}{3}M_{11}(M_{03} - M_{30})$  [59,60], allowing for the latter term to be neglected in favor of a simpler, “incomplete” CEM. However, the skewness terms are retained here for completeness. As a bridge to the failure of K-theory, a large corpus of experiments on momentum transport over smooth surfaces and differing types of roughness elements suggest a linear relation between each of the third-order moments. Specifically,  $M_{30} = b_u M_{12}$ ,  $M_{03} = b_w M_{12}$ , and  $M_{21} = b_{uw} M_{12}$  where the respective constant values  $b_u \approx 2$ ,  $b_w \approx -1.16$ , and  $b_{uw} \approx -1$  were presented elsewhere [9]. The value  $b_{uw} \approx -0.6$  was also reported for flows within and just above dense canopies across a wide range of thermal stratification conditions [24,27]. The validity of the linear relation and the values for the constants  $b_{u,w,uw}$  are evaluated in Sec. IV. Inserting these linear relations into Eq. (11) yields

$$M_{12} \approx \frac{2\sqrt{2\pi}}{\frac{1}{3}M_{11}(b_w - b_u) + (b_{uw} - 1)} M_{11} \Delta S_o. \quad (12)$$

For  $b_u \approx 2$ ,  $b_w \approx -1.16$ ,  $b_{uw} \approx -1$ , and  $M_{11} \approx -0.45$ , which is typical in turbulent boundary layers, Eq. (12) yields a value  $M_{12} \approx -1.5\Delta S_o$  consistent with prior wind tunnel experiments over various roughness types [9]. Using the definitions for  $M_{ij}$ , Eq. (12) is given in dimensional form as

$$\overline{u'w'w'} \approx \frac{2\sqrt{2\pi}}{\frac{1}{3}M_{11}(b_w - b_u) + (b_{uw} - 1)} \overline{u'w'} \sigma_w \Delta S_o, \quad (13)$$

which is a *structural closure model* for the flux transport term resembling  $F_{\text{TKE}}$  in Eq. (2). As noted above, the direct contribution from the skewnesses  $\frac{1}{3}M_{11}(b_w - b_u) \approx 0.45$  is smaller than that of the mixed moments  $(b_{uw} - 1) \approx -2$ . The form of Eq. (13) suggests that  $\overline{u'w'w'}$  is proportional to  $\sigma_w \overline{u'w'}$ , not the stress gradient as assumed in conventional gradient-diffusion closure arguments expressed as [45]

$$\overline{u'w'w'} \propto -\ell_m(\bar{e})^{1/2} \frac{\partial \overline{u'w'}}{\partial z}. \quad (14)$$

When ejections and sweep contribute equally to momentum transport,  $\Delta S_o = 0$  and  $\overline{u'w'w'} = 0$ . That is, symmetry in momentum flux transport and validity of K-theory appear to be “entangled.”

## 2. Model 2: Streamwise velocity asymmetry

In a separate approach, the Gram-Charlier expansions can also be used to establish a link between the stress transport and asymmetry in the streamwise velocity distribution pdf( $u$ ). Because of the connection between the streamwise velocity distribution and  $\overline{u'w'w'}$  through the relation  $M_{30} = b_u M_{12}$ , the structural model can be cast with respect to the fraction of time with  $u' < 0$  (slow flow) or  $u' > 0$  (fast flow) instead of with respect to the entire stress fraction. To illustrate, the fraction of time the flow resides in a faster-than-average phase ( $u' > 0$ ) is

$$\Gamma_+ = \int_0^\infty \text{pdf}(\hat{u}) d\hat{u}, \quad (15)$$

where  $\text{pdf}(\hat{u})$  is the probability density function of the standardized velocity  $\hat{u} = u'/\sigma_u$ , i.e., where  $\sigma_{\hat{u}} = 1$ . The parameter  $\Gamma_+$  quantifies the distribution asymmetry, with  $\Gamma_+ > 0.5$  indicating more weak fast phases ( $u' > 0$ ) which are balanced by a longer low-velocity tail than the symmetric case, yielding negative skewness. Oppositely,  $\Gamma_+ < 0.5$  corresponds to a longer high-velocity tail and positive skewness. To solve for  $\Gamma_+$ , a third-order Gram-Charlier cumulant expansion is used to describe  $\text{pdf}(\hat{u})$  as

$$\text{pdf}(\hat{u}) = G(\hat{u}) \left[ 1 + \frac{1}{6} M_{30} (\hat{u}^3 - 3\hat{u}) \right], \quad G(\hat{u}) = \frac{1}{\sqrt{2\pi}} \exp \left[ -\frac{1}{2} \hat{u}^2 \right], \quad (16)$$

where  $G(\hat{u})$  is a standard Gaussian distribution. Evaluating the integral in Eq. (15) using the expansion in Eq. (16) leads to the relation [59,61]

$$\Gamma_+ = 0.5 - \frac{1}{12} \sqrt{\frac{2}{\pi}} M_{30}. \quad (17)$$

With  $M_{30} = b_u M_{12}$  and  $b_u$  independent of roughness [9], Eq. (17) can be rearranged as

$$M_{12} = (0.5 - \Gamma_+) \frac{12}{b_u} \sqrt{\frac{\pi}{2}}, \quad (18)$$

so that the simplified structural model is cast in fast-slow phases of  $u'$  instead of an ejection-sweep imbalance as

$$\overline{u'w'w'} \approx \frac{6\sqrt{2\pi}}{b_u} \sigma_u \sigma_w^2 (0.5 - \Gamma_+). \quad (19)$$

Equations (17)–(19) remain unchanged even when a fourth-order Gram-Charlier cumulant expansion is adopted for  $\text{pdf}(\hat{u})$ . The experiments described next in Sec. III evaluate the applicability of these two structural models given in Eqs. (13) and (19) and assess to what degree the parameters depend on surface roughness and Reynolds number. The choice of using  $u'$  instead of  $w'$  for  $\Gamma_+$  will be elaborated upon when discussing the validity of CEM. Briefly, it will be shown that the probability distribution of  $w'$  is more symmetric than the  $u'$  counterpart, but with higher excess kurtosis. Hence, measures of asymmetry are better captured by  $u'$  instead of  $w'$ .

### III. EXPERIMENTS

#### A. Flow measurements

The present analysis was conducted on previously published numerical and experimental datasets summarized in Table I. The collection of turbulent boundary layer measurements span approximately one order of magnitude in Reynolds number across multiple surface geometries, thus providing a range in parameter space to evaluate the structural models introduced in Sec. II B. The friction Reynolds number in Table I is defined as  $\text{Re}_\tau = \delta u_\tau / \nu$ , where  $\delta$  is the boundary layer thickness. The thickness  $\delta$  is taken to be the height where the mean velocity is 99% of the free-stream value, i.e.,  $\delta = z(U = 0.99U_\infty)$ . For rough-wall conditions, the surface roughness is parameterized using the equivalent sandgrain roughness  $k_s$  and the roughness height  $k$ . Determination of the flow and surface parameters is detailed in the referenced source for each case.

The lowest Reynolds number case in smooth-wall conditions is the DNS of Sillero *et al.* [62]. The DNS case is included to validate the profiles obtained from experiments. The two additional smooth-wall cases and the woven wire mesh cases were collected in the boundary layer wind tunnel at St. Anthony Falls Laboratory (SAFL), University of Minnesota. The SAFL experiments include cross-hotwire anemometry measurements of  $u$  and  $w$  across the full boundary layer thickness, and complementary particle image velocimetry (PIV) measurements in the lowest 10 cm (25% of  $\delta$  in the mesh cases) [56]. The hotwire measurements are featured in later figures showing wall-normal profiles of the boundary layer, while the PIV results are used for direct comparison of model

TABLE I. Overview of smooth- and rough-wall boundary layer experiments used in the present analysis. The cases span a range of friction Reynolds number  $Re_\tau = \delta u_\tau / \nu$  and roughness Reynolds number  $k_s^+ = k_s u_\tau / \nu$ , where  $\delta$  is the boundary layer thickness,  $u_\tau$  is the friction velocity,  $\nu$  is the kinematic viscosity, and  $k_s$  is the equivalent sandgrain roughness.

Data set	Symbol	$Re_\tau$	$k_s^+$	$k_s/\delta$	$k/\delta$	Source
Smooth wall DNS	—	2000	—	—	—	Sillero <i>et al.</i> [62]
Smooth wall 1	×	3800	—	—	—	Heisel <i>et al.</i> [56]
Smooth wall 2	+	4700	—	—	—	Heisel <i>et al.</i> [56]
Cylinders 1	○	8200	710	0.087	0.050	Raupach <i>et al.</i> [63]
Cylinders 2	◇	9000	840	0.094	0.048	Raupach <i>et al.</i> [63]
Woven mesh 1	△	10 100	430	0.043	0.015	Heisel <i>et al.</i> [56]
Woven mesh 2	▽	13 900	620	0.045	0.015	Heisel <i>et al.</i> [56]
Sandpaper 1	◁	12 100	64	0.0053	0.0025	Squire <i>et al.</i> [64]
Sandpaper 2	▷	18 400	104	0.0056	0.0026	Squire <i>et al.</i> [64]

parameters due to a greater number of data points within the RSL. The rough-wall hotwire and PIV measurements were taken at multiple positions within the woven mesh pattern to provide a representative horizontal spatial average in the RSL.

The two cylinder roughness cases are from previous experiments in the University of Edinburgh wind tunnel. These cases were digitized from results presented in both Raupach *et al.* [63] and Raupach [9]. The cylinder roughness results are limited to the statistics presented in the original studies; some cases were excluded from later figures because the published data were not available.

Finally, flow above sandpaper surface roughness was measured using PIV in the High Reynolds Number Boundary Layer Wind Tunnel at the University of Melbourne. These measurements used a high-spatial-resolution tower PIV configuration and were introduced in Squire *et al.* [64]. Detailed parametrization of the sandpaper roughness geometry is given in a separate study [65].

While all of the rough-wall cases evaluated here are considered fully rough, the sandpaper cases are closest to the upper limit of transitional roughness in terms of  $k_s^+$ . The roughness length  $k$  is given here by the approximate total height of the roughness geometry. Dimensionally, the heights are  $k = 6$  mm (cylinders and woven mesh) and  $k = 0.9$  mm (sandpaper). For rough-wall and canopy flows, the zero-displacement position ( $z-d$ ) is commonly used to account for the shift in the boundary layer away from the wall due to the surface asperities. For the woven mesh cases,  $d$  was assumed to correspond to the average roughness height across the mesh geometry. For the sandpaper cases,  $d$  was taken as half the roughness height [65]. The  $d$  for the cylinder cases was reported directly in Raupach *et al.* [63].

## B. Flow statistics

Wall-normal profiles of the first- and second-order velocity statistics are featured in Fig. 1. The normalization of the profiles, i.e., by  $u_\tau$  and  $\delta$ , reflects the relevant turbulent scaling parameters in the outer layer above the RSL and buffer layer. In this work, the superscript “+” for velocity statistics indicates normalization by  $u_\tau$ . There is generally good agreement in the outer layer velocity statistics across flow cases, with the exception noted below.

The primary discrepancy observed in Fig. 1 is lower measured values of  $\overline{w'^2}$  and  $\overline{u'w'}$  for the smooth-wall experiments (×, +). These values may be underestimated due to the spatial sampling volume of the Dantec hotwire X probe used for the smooth-wall and woven mesh experimental cases. The “X” shape of the two wires and their separation distance yield a sampling volume that is  $O(1$  mm) ( $\approx 25$  viscous units) in each direction. The underestimated  $w$  statistics may be attributed to undetected turbulent motions smaller than the sampling volume. The underestimate is lesser for the streamwise statistics for which a greater proportion of energy resides in the larger scales.



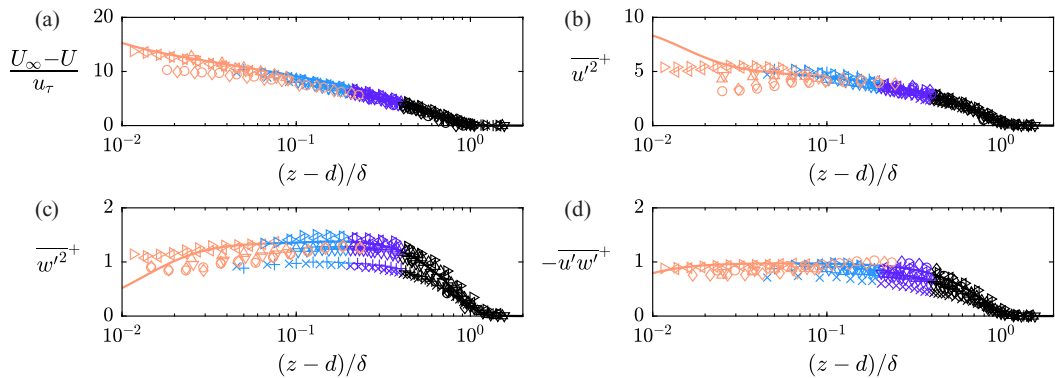


FIG. 1. Wall-normal profiles of first- and second-order velocity statistics normalized by the friction velocity  $u_\tau$  and boundary layer thickness  $\delta$ : (a) deficit of the mean velocity  $U$  from the free-stream  $U_\infty$ ; (b) streamwise variance  $\overline{u'^2}$ ; (c) wall-normal variance  $\overline{w'^2}$ ; (d) turbulent shear stress  $\overline{u'w'}$ . The data symbols, shown with logarithmic spacing for clarity, correspond to the cases in Table 1. Colors here and in later figures correspond to the buffer or roughness sublayer (orange), logarithmic region (blue), transition from logarithmic to wake region (purple), and outer wake region (black).

The sampling volume is also less limiting for the mesh cases due to the near-wall behavior being governed by the roughness geometry rather than the relatively smaller viscous units.

Based on later results, the measurement resolution does not affect the model performance. This suggests the model outcome and inputs have similar scale dependence and are limited by resolution to the same extent. In other words, underestimates in the measured  $\overline{u'w'w'}$  model output may be balanced by likewise underestimates in the inputs  $\overline{w'^2}$  and  $\overline{u'w'}$ .

In Fig. 1 and throughout, the following color-coded convention of the four main regions of the turbulent boundary layer is adopted: (1) RSL and viscous buffer layer below the log region (orange); (2) the log region up to  $0.2\delta$  (blue); (3) the lower portion of the wake region where there is a slow departure from inertial behavior and  $z$  scaling of the flow statistics, up to  $0.4\delta$  (purple); and (4) the outer portion of the wake region (black). The extent of the buffer layer in smooth-wall conditions was taken to be approximately  $3\sqrt{\delta}v/u_\tau$  [66]. The RSL was assumed to end where inertial dynamics and the log region began in the Fig. 1 velocity statistics and third-order moments introduced later. Previous studies have shown third-order statistics to be a good indicator for the extent of roughness and canopy effects [21]. Based on trends in these higher-order statistics, the RSL height for the cylinder cases is approximately  $z_{\text{RSL}} \approx 0.25\delta$ . Thus, there is no canonical log region for the cylinder cases. This absence has no bearing on the evaluation of the structural models.

The delineation of the wake region into two portions is due to the turbulent/nonturbulent interface (TNTI) separating boundary layer turbulence from the free-stream condition. In instantaneous flow fields, the TNTI can reach positions as low as the selected division point  $z/\delta = 0.4$  in high-Reynolds-number conditions [67]. A strong decrease in the turbulent statistics in the outer wake is apparent in Fig. 1. The effect of the free-stream condition on higher-order statistics (e.g.,  $M_{ij}$ ) and the structural model introduced above is not the main focus of the present work. We purposely exclude the outer wake from later figures, except for wall-normal profiles where the outer wake is easily distinguished from the other regions.

Figure 2 features the measured wall-normal profiles of  $M_{30}$  (streamwise velocity skewness),  $M_{03}$  (wall-normal velocity skewness),  $M_{12}$  (momentum flux transport), and  $M_{21}$  (streamwise variance transport) using the same color coding as Fig. 1 for the regions. There is close agreement between the DNS results and the experimental cases throughout the boundary layer, except for the RSL where a deviation is to be expected. Each  $M_{ij}$  profile exhibits the same trend: the moment is close to zero and relatively constant in the log region, the value increases significantly in the low-turbulence



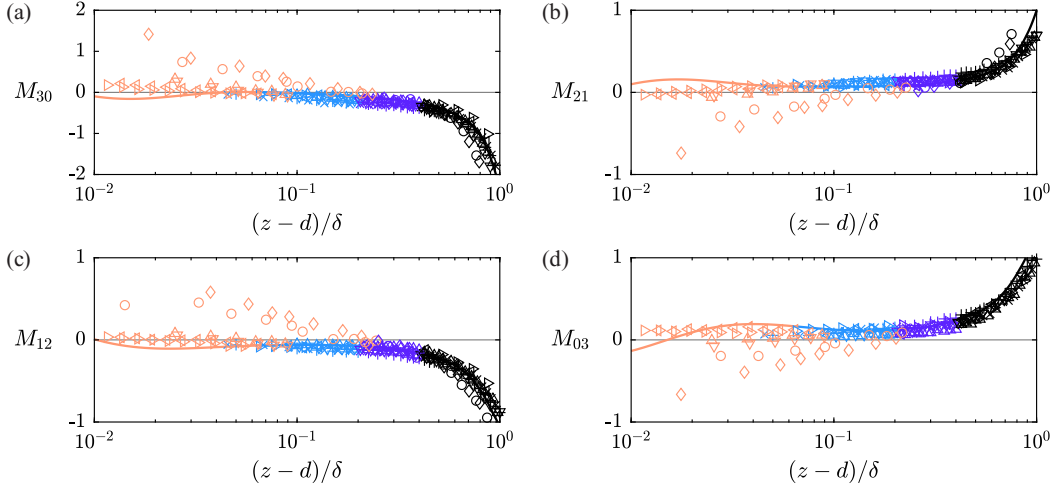


FIG. 2. Wall-normal profiles of third-order statistical moments  $M_{ij}$  of the velocity fluctuations, where  $i$  corresponds to the order of  $u'$  and  $j$  corresponds to  $w'$  as defined in Eq. (10). The data symbols, shown with logarithmic spacing for clarity, correspond to the cases in Table I.

outer wake, and there is a switch in asymmetry direction (i.e., sign) in the RSL. The change in sign is not observed for  $M_{03}$  for the sandpaper cases in Fig. 2(d). This discrepancy is discussed further with respect to a later figure.

The extensive RSL for the cylinder roughness ( $\circ$ ,  $\diamond$ ) is visually apparent in Fig. 2, where close agreement with the remaining cases is observed only above  $0.25\delta$ . The  $M_{ij}$  profiles transition directly from the RSL trend to the wake region behavior, and no log region is apparent as noted previously. There is likely insufficient scale separation, i.e., large  $k/\delta$  in Table I, for a canonical overlap layer (log region) to develop [68].

The measured  $\Delta S_o$  profile derived from quadrant analysis for all cases is presented in Fig. 3. The  $\Delta S_o$  profile shows remarkable collapse in the outer layer, consistent with other studies [8,9]. The collapse is also consistent with Townsend's outer layer similarity [52,69], where the surface conditions have negligible effect on the stress contributions in the log and wake regions.

As expected from the previously discussed literature, sweep events are the majority contributor to  $\overline{u'w'}$  in the RSL ( $\Delta S_o > 0$ ), and ejections are dominant in the wake ( $\Delta S_o < 0$ ). The constant value in the log region ( $\Delta S_o \approx -0.1$ ) indicates ejections contribute more than sweeps, but the magnitude of both contributions is roughly comparable. There is no Reynolds number trend in the fractional stress contribution  $\Delta S_o$ . The result suggests a composite profile for  $\Delta S_o(z)$  is possible, however a wider range of rough-wall experiments is required to parametrize the profile behavior in the RSL.

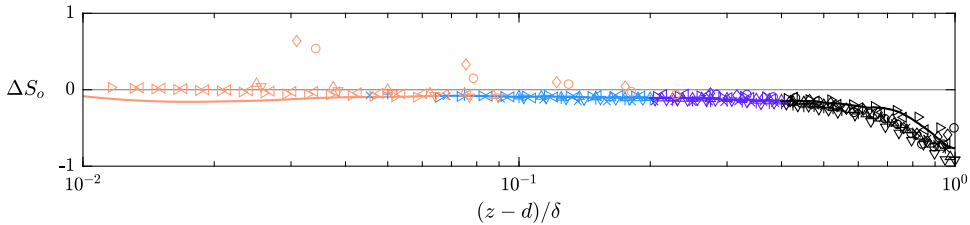


FIG. 3. Wall-normal profile of  $\Delta S_o$  defined in Eq. (7) by the fractional contribution of ejections ( $u' < 0$ ,  $w' > 0$ ) and sweeps ( $u' > 0$ ,  $w' < 0$ ) to the turbulent shear stress  $\overline{u'w'}$ . Data symbols correspond to the cases in Table I.

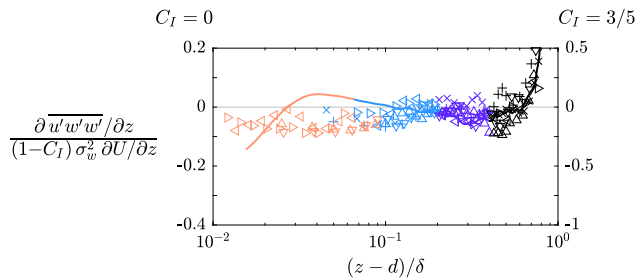


FIG. 4. Ratio of the transport and production terms contributing to the momentum flux in Eq. (6). Gradient-diffusion closure (K-theory), which neglects transport, is valid when the ratio is small. The left vertical axis is based on  $C_I = 0$  (no isotropization) and the right  $C_I = 3/5$  (isotropization predicted by rapid distortion theory).

The wall-normal trend in  $\Delta S_o$  closely mirrors the  $M_{ij}$  trends in the RSL, log region, and wake region. The qualitative similarity in the profiles is consistent with the dependence of  $\Delta S_o$  on the moments  $M_{ij}$  described in the CEM of Eq. (11), and suggests asymmetry in  $u$  and  $w$  is closely related to the stress contributions quantified by  $\Delta S_o$ . In the following section, the  $M_{ij}$  and  $\Delta S_o$  statistics are analyzed in closer detail to assess the structural models for  $\overline{u'w'w'}$ .

#### IV. RESULTS

The results are presented in four subsections: the relative importance of transport to the shear stress budget is first considered in the various regions to illustrate where the flux-transport can be significant. The third-order CEM approximation and its utility in estimating  $\Delta S_o$  is then evaluated. The assumptions employed in the derivation of the model as well as the dependence (or lack thereof) of the coefficients  $b_{u,w,ww}$  on Reynolds number and roughness are then featured. Last, the structural models are evaluated by comparing the model estimates against measurements of  $\overline{u'w'w'}$  for each flow case.

##### A. Significance of turbulent stress transport

A central consideration of the present work is the relative contributions of the production and transport terms to the shear stress in Eq. (6). Gradient-diffusion closure models and K-theory are only valid when the transport  $\partial \overline{u'w'w'}/\partial z$  is small relative to the production  $(1 - C_I)\sigma_w^2 \partial U/\partial z$ . Rather than calculate the full expression in Eq. (6), which requires an estimate of the relaxation time, Fig. 4 shows a ratio of the measured transport and production terms to evaluate their relative contributions. The vertical axes are scaled using two values for  $C_I$ . The values provide approximate bounds for the production term estimate, where  $C_I = 0$  indicates no isotropization of the production and  $C_I = 3/5$  is the value predicted by rapid distortion theory [53].

As expected, the ratio is small, i.e., less than 10%, within the logarithmic region where K-theory applies [50,52,53,70]. Transport is non-negligible in the RSL, however, where its contribution is 10%–25% of the production for the woven mesh depending on choices made about  $C_I$ . These estimates are close to values reported for a rod canopy at very high Reynolds numbers [22]. Note that ratios larger than 25% may be observed closer to (and within) the roughness canopy or for other roughness geometries.

Figure 4 confirms turbulent transport cannot be discarded in the closure of the stress budget within the RSL and also in the outer wake. A useful analogy can be drawn to the much-studied TKE budget: the log region is a form of equilibrium layer where there is negligible net wall-normal transport of energy, referred to as nonlocal transport in atmospheric applications. Outside the log region, the nonequilibrium is marked by net transport of TKE and also shear stress as seen in Fig. 4.

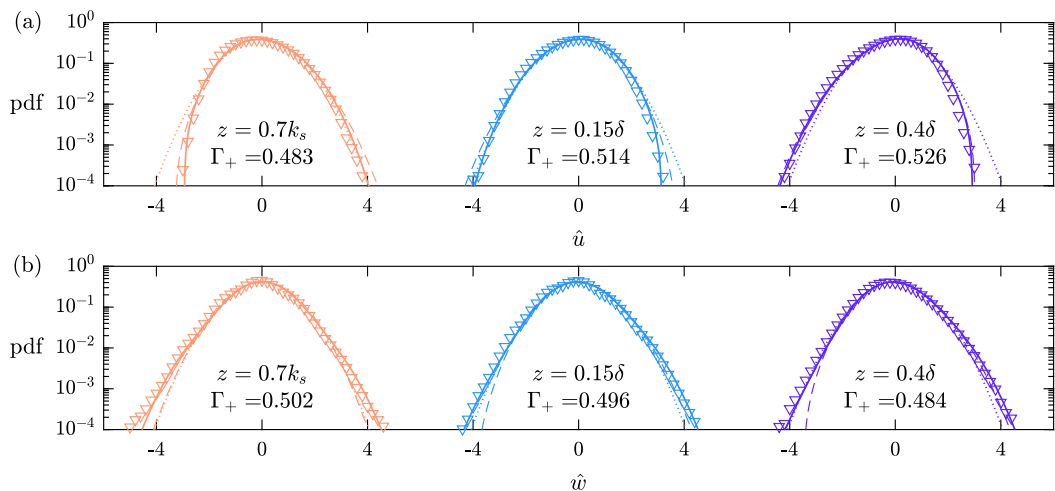


FIG. 5. Example probability density functions (pdfs) of velocity fluctuations from the  $Re_\tau = 13\,900$  rough-wall case at three wall-normal positions: (a)  $\hat{u} = u'/\sigma_u$  and (b)  $\hat{w} = w'/\sigma_w$ . The measured distribution is compared with a Gaussian distribution ( $\cdots$ ), third-order CEM ( $-\ -$ ), and fourth-order CEM ( $—$ ) based on the measured statistical moments used in the calculations of cumulants.

In this sense, the roughness sublayer extent may be defined as the wall-normal distance required to distribute (through transport) the stress imparted by the roughness before equilibrium conditions can be reached. This definition has been used to delineate the CSL in flow over rod canopies situated on hilly terrain [15].

### B. Validity of the third-order CEM

Example probability distributions of  $\hat{u}$  and  $\hat{w}$  are shown in Fig. 5 for the RSL (left), log region (middle), and wake region (right). The measured probabilities are compared with a Gaussian distribution, third-order CEM (used in the later analysis), and fourth-order CEM. The distribution asymmetry is clearly apparent in the streamwise component  $\hat{u}$  in Fig. 5(a). The asymmetry is reflected by the listed  $\Gamma_+$  values and is accounted for by the third-order CEM. The wall-normal velocity  $\hat{w}$  in Fig. 5(b) is roughly symmetric and does not deviate appreciably from Gaussian, except in the thickness of the probability tails that is accounted for by the fourth-order CEM. While the fourth-order CEM modestly improves agreement with the measured pdf, the third-order CEM is sufficient for describing asymmetry trends (e.g., as discussed for Figs. 2 and 3) and linking  $\Gamma_+$  with  $\overline{u'w'w'}$  in the structural model. Specifically, the fourth-order cumulant terms, in addition to any other even-order cumulants, cancel out from the expression for  $\Gamma_+$  in Eq. (17) as earlier noted.

Instead of evaluating the CEM for joint pdfs of  $u'$  and  $w'$ , Fig. 6 directly compares the prediction of  $\Delta S_o$  from Eq. (11) with measurements of  $\Delta S_o$  from Fig. 3. Given the high coefficient of determination  $R^2 = 0.96$ , the CEM in Eq. (11) closely predicts the observed  $\Delta S_o$  value. The agreement between the measurements and the third-order cumulant expansion demonstrates the ability of the CEM to capture the essential features in the joint pdf of  $u'$  and  $w'$  needed to predict  $\Delta S_o$ . These features are quantified through the third-order moments  $M_{ij}$ , which are further evaluated in the following subsection. The success of the third-order CEM in Fig. 6 is consistent with prior studies that showed the CEM prediction of  $\Delta S_o$  to agree well with measurements for canopy flows on flat and complex terrain, stratified atmospheric surface layer flows, and even flow below ice sheets [15,16,22,24,36,60].

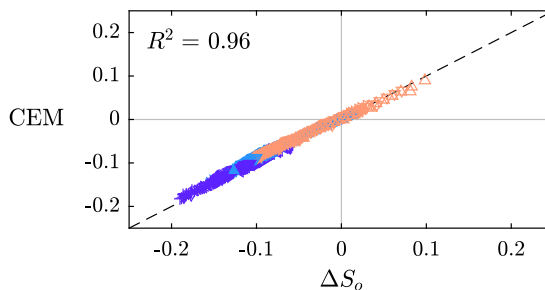


FIG. 6. Comparison of the measured stress fraction  $\Delta S_o$  with predictions by the third-order cumulant expansion in Eq. (11). The dashed line (---) is a 1:1 relation indicating a correct prediction. Data symbols correspond to the cases in Table I, where the outer wake region is excluded.

### C. Links between $M_{ij}$ , $\Delta S_o$ , and $\Gamma_+$

One of the key results of Raupach [9] was the observed linear relations between all the third-order mixed moments  $M_{ij}$  related to  $u'$  and  $w'$ . Raupach [9] additionally suggested a linear relation between  $M_{ij}$  and  $\Delta S_o$ , consistent with the CEM prediction in Eq. (11) if  $M_{11}$  is constant. Figure 7 evaluates the relations between the third-order moments  $M_{ij}$ , including for two cylinder cases ( $\circ$ ,  $\diamond$ ) from the original study [9]. The figure confirms the linear relations between  $M_{ij}$  for a wider range of roughness geometry and Reynolds numbers.

The 95% statistical confidence intervals for each  $M_{ij}$  statistic are represented by the example error bars in Fig. 7. The intervals were estimated from the mesh PIV cases using a bootstrap resampling method [71]. The statistical uncertainty is due primarily to the number of independent samples, i.e., PIV frames, and varies minimally with wall-normal distance or between the mesh and smooth-wall cases. The intervals demonstrate the mixed products  $M_{21}$  and  $M_{12}$  have less uncertainty and are more converged statistically than the skewnesses. Moderate scatter is observed for  $M_{03}$  across cases, where the wall-normal skewness remains positive for the sandpaper data in the RSL as previously noted. However, this scatter is comparable to the confidence intervals and is not interpreted here as a physical effect of the roughness.

Aside from this scatter, the consistency of the trends in Fig. 7 for a range of Reynolds number and surface properties (i.e., smooth, cylinders, woven mesh, sandpaper) suggests the slope parameters  $b_{u,w,uw}$  are invariant and there is a generic similarity in the third-order moment relations. While the roughness properties influence the magnitude of  $M_{ij}$  within the RSL as seen in Fig. 2, the same relation between the statistics is maintained. The results therefore support the structural model

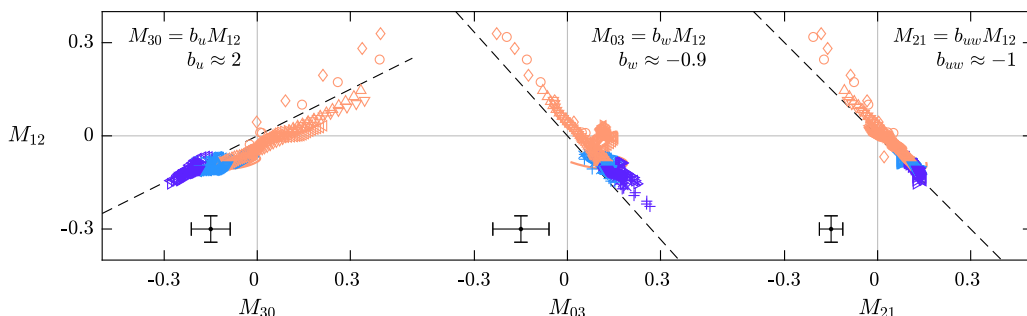


FIG. 7. Linear relations between the third-order moments  $M_{ij}$  in the roughness sublayer and logarithmic regions. Dashed lines (---) represent the linear relations given by Raupach [9]. The error bars are estimated 95% confidence intervals for the mesh PIV cases. Data symbols correspond to the cases in Table I.

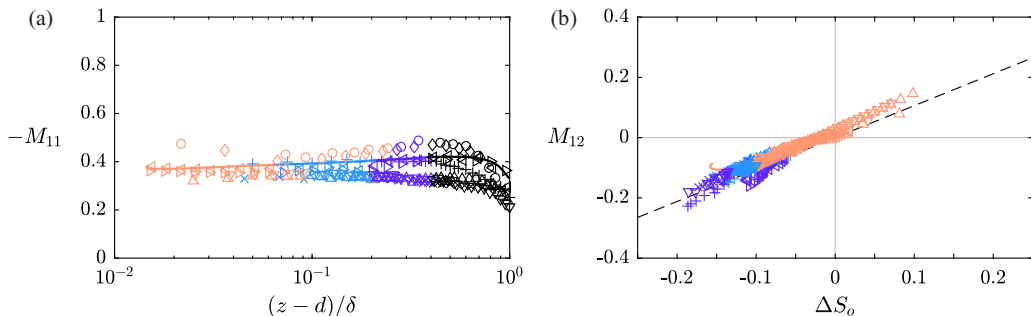


FIG. 8. Behavior of the parameters  $M_{11}$  and  $\Delta S_o$  in Eq. (12). (a) Wall-normal profile of the correlation coefficient  $M_{11}$  for  $(u', w')$ . (b) Approximate linear relation between  $M_{12}$  and  $\Delta S_o$  where the dashed line (---) is  $M_{12} = -1.05\Delta S_o$ . Data symbols correspond to the cases in Table I, where the outer wake region is excluded from (b).

simplification in Eq. (12), where the linear relations are used to express the model in terms of  $\Delta S_o$  and  $M_{21}$ . The observed similarity may in part be due to similar coherent eddy structure in high-Reynolds-number roughness sublayers; recent simulations found the sublayer to be populated by diffuse larger-scale roller structures which are prominent in the inertial layer [72].

Linear regression fits were used to prescribe parameters  $b_{u,w,uw}$ . However, the resulting values depended on which regions of the boundary layer were included in the fit and whether the separate fits were conducted on each data set (due to small nonzero intercepts for certain cases). At this time it is unknown whether the intercepts are a physical result or an artifact of the experiments. For  $M_{21} = b_u M_{30}$  and  $M_{12} = b_{uw} M_{21}$  there was no statistically significant difference from  $b_u \approx 2$  and  $b_{uw} \approx -1$  [9]. A larger difference was observed for the fitted value  $b_w \approx -0.9$  compared to the original finding  $b_w = -1.16$ . The most likely reason for the difference is the outer wake region behavior as discussed in Sec. III B. There is a shift in the linear trends between  $M_{ij}$  in the outer wake region, which we attribute to the influence of the free-stream condition on the flow statistics and is the reason this region is excluded from the results. In contrast, the fitted relations in Raupach [9] included points throughout a majority of the boundary layer thickness, such that these previous relations may be affected somewhat by the distinct outer wake behavior.

In addition to the parameters  $b_{u,w,uw}$ , the structural model for  $M_{12}$  in Eq. (12) includes the correlation  $M_{11}$  and stress fraction  $\Delta S_o$  that are evaluated in Fig. 8. Wall-normal profiles of  $M_{11} = \overline{u'w'}/\sigma_u\sigma_w$  are shown in Fig. 8(a). If outer layer similarity applies to  $\overline{u'^2}$ ,  $\overline{w'^2}$ , and  $\overline{u'w'}$ , then similarity should also extend to  $M_{11}$  in the outer layer. The values in Fig. 8(a) are in good agreement with the previous cylindrical cases with  $M_{11} \approx -0.45$  [9], and the observed differences between cases may be due to experimental uncertainties. The DNS profile suggests  $M_{11}$  decreases moderately from  $-0.35$  to  $-0.4$  across the log region. This trend is consistent with theoretical velocity profiles, i.e., streamwise variance decreasing logarithmically, constant wall-normal variance and turbulent shear stress [69]. Due to the  $z$ -dependent trend in the log region, in addition to possible geometry-specific decorrelating effects in the RSL, the  $M_{11}$  profile is an input for the structural model and is not assumed to be a constant parameter except where noted.

If  $M_{11}$  is assumed to be constant, a linear relation between  $M_{12}$  and  $\Delta S_o$  emerges from Eq. (12). A comparison of  $M_{12}$  and  $\Delta S_o$  is shown in Fig. 8(b). The approximation of the simplified linear relation appears valid, which follows from the relatively constant  $M_{11}$  profile in Fig. 8(a). The slope of the dashed line in Fig. 8(b) results from Eq. (12) with the  $b_{u,w,uw}$  values listed in Fig. 7 and the approximate coefficient  $M_{11} \approx -0.35$ . The estimate aligns well with the observed comparison, and the model prediction is further evaluated in the next section.

The central parameter of the second structural model is the asymmetry metric  $\Gamma_+$  shown in Fig. 9. The figure compares the relation between  $\Gamma_+$  and the velocity skewnesses with the CEM prediction

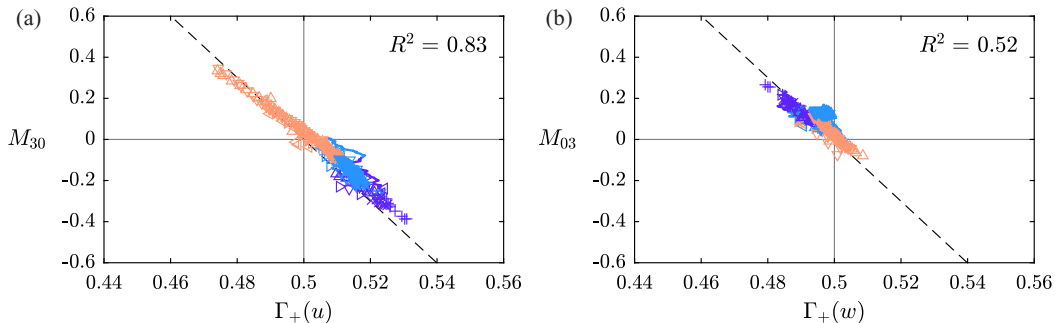


FIG. 9. Relation between  $\Gamma_+$  and the skewness of velocity fluctuations. (a) Comparison of  $\Gamma_+(u)$  and streamwise skewness  $M_{30}$ . (b) Comparison of  $\Gamma_+(w)$  and wall-normal skewness  $M_{03}$ . The dashed lines (---) are the expression in Eq. (17). Data symbols correspond to the cases in Table I, where the outer wake region is excluded.

in Eq. (17). As expected, the agreement is better for the  $u$  component in Fig. 9(a) when compared to the  $w$  component in Fig. 9(b) given that the pdf of  $u$  experiences greater asymmetry. The agreement between the third-order CEM and measurements of  $M_{30}$  and  $\Gamma_+$  is encouraging and suggests that roughness geometry may not impact the relation between  $\Gamma_+$  and  $M_{30}$ . Taking this result together with the relation between  $M_{12}$  and  $M_{30}$  in Fig. 7, the coefficient  $b_u = 2$  is also deemed insensitive to surface roughness as it applies to the second structural model in Eq. (18).

#### D. Evaluating the two structural models

The evidence thus far suggests the linear relations between  $M_{ij}$ ,  $\Delta S_o$ , and  $\Gamma_+$  are robust, and the model coefficients  $b_{u,w,uw}$  appear independent of the Reynolds number and roughness geometry, even within the RSL. Having evaluated the individual parameters, the present section compares the two proposed structural models against direct measurements of  $\overline{u'w'w'}$ . Recall the first structural model in Eq. (13) is based on  $\Delta S_o$  while the second in Eq. (19) is based on  $\Gamma_+$  (derived from the streamwise velocity component  $u'$  only). Rather than evaluating the models in terms of the statistical moments, e.g.,  $M_{12}$ , we normalize both the structural models and the measurements of  $\overline{u'w'w'}$  by  $u_*^3$ . With this normalization, the structural models are expressed as

$$\overline{u'w'w'}^+ \approx \frac{2\sqrt{2\pi}}{\frac{1}{3}M_{11}(b_w - b_u) + (b_{uw} - 1)} \overline{u'w'}^+ \sigma_w^+ \Delta S_o \approx \frac{6\sqrt{2\pi}}{b_u} \sigma_u^+ \overline{w'w'}^+ (0.5 - \Gamma_+). \quad (20)$$

The performance of the two structural models is shown in Figs. 10(a) and 10(b). There is close agreement between the model prediction and the measurements as indicated by the high coefficient of determination ( $R^2$ ) values of the comparison. A majority of the model error appears to be due to a small offset between the model and the measurements. The offset may be related to the small nonzero intercept observed in previous linear relations such as in Fig. 7. Note that the offset has no effect on the gradient  $\partial \overline{u'w'w'}^+ / \partial z$ , which is ultimately the term of interest in the momentum flux budget. Visually, the  $\Delta S_o$  structural model appears more accurate in the RSL, though the  $R^2$  value is comparable for both models.

In the log region, the profiles of  $\overline{u'w'}^+(z) \approx -1$  and  $\sigma_w^+(z) \approx 1.1$  are relatively constant both in theory and in the Fig. 1 measurements. Taking these values with  $M_{11} \approx 0.35$  and the fitted  $b_{u,w,uw}$  values, further model approximations yield the simplified expressions

$$\overline{u'w'w'}^+ \approx 2.36 \Delta S_o \approx 9.1 \sigma_u^+ (0.5 - \Gamma_+). \quad (21)$$



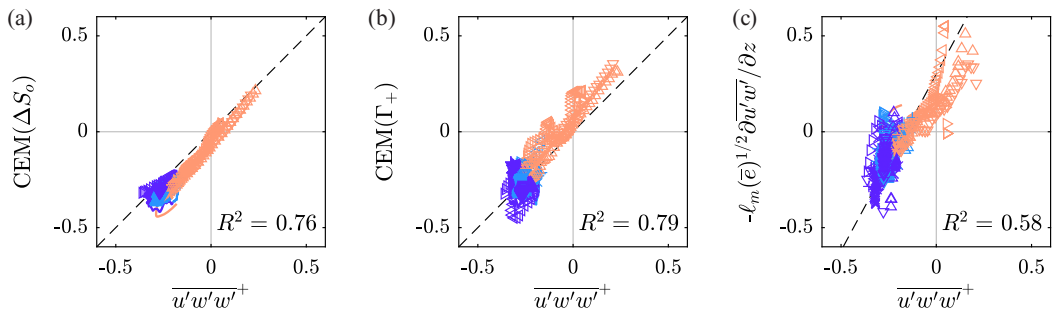


FIG. 10. Comparison between modeled and measured momentum flux transport term  $\overline{u'w'w'}$ . For the two proposed structural models, the constants are  $b_u = -2$ ,  $b_w = -0.9$ , and  $b_{uw} = -1$ . (a)  $\Delta S_o$  model in Eq. (13); (b)  $\Gamma_+$  model in Eq. (19); (c) traditional gradient-diffusion model in Eq. (14) is added for reference. Each axis is normalized by  $u_\tau^3$ . The dashed lines (- -) are 1:1 relations indicating a correct prediction, except for (c) where the dashed line is a linear regression. Data symbols correspond to the cases in Table I, where the outer wake region is excluded.

That is, the transport term  $\overline{\partial u'w'w'}/\partial z$  is primarily driven by changes in asymmetry quantified by  $\partial \Delta S_o/\partial z$  or  $\partial \Gamma_+/\partial z$ . These gradients are small in the log region, as seen in Figs. 3 and 10(a), but can be large within the RSL or even the viscous buffer region, which was studied here in less detail. While the approximated constants  $\overline{u'w'w'^+} \approx -1$  and  $\sigma_w^+ \approx 1.1$  appear to match RSL measurements for the present rough-wall cases, the near-wall behavior of  $\overline{u'w'}$  and  $\sigma_w$  is likely modified by the roughness, especially closer to the roughness canopy, which was not measured here. These constants in Eq. (21) provide a simpler form of the structural models than in Eq. (20), but the simplification is likely at the expense of predictive accuracy in the RSL.

To emphasize the skill of the proposed structural models, the traditional gradient-diffusion closure in Eq. (14) is evaluated for comparison in Fig. 10(c). The comparison uses the mixing length  $\ell_m = \kappa z$  in the log region and  $\ell_m = \kappa z_{\text{RSL}}$  (a constant) in the RSL, where  $z_{\text{RSL}}$  is the height of the roughness layer. The average TKE was estimated as  $\bar{e} = \frac{1}{2} \times \frac{3}{2} (\overline{u'^2} + \overline{w'^2})$  for the experimental cases where the spanwise velocity component  $v$  was not measured. Due to the proportional relation in Eq. (14), the prediction was evaluated using a linear regression to data points in the log region rather than a direct comparison against  $\overline{u'w'w'^+}$ . A finite bias is apparent in the gradient-diffusion closure: the measured  $\overline{u'w'w'}$  is nonzero where  $\overline{\partial u'w'}/\partial z \approx 0$ , leading to a nonzero intercept. This bias is accounted for in the structural models that correctly predict the location for  $\overline{u'w'w'} = 0$  in Fig. 10(a,b). Whereas the structural models predict  $\overline{u'w'w'}$  within the RSL, the gradient-diffusion closure for  $\overline{u'w'w'}$  deviates appreciably from measurements, likely in part due to the need for a more realistic estimate of  $\ell_m(z)$  in this region. Unlike  $\ell_m(z)$ , the structural model parameters  $b_{u,w,uw}$  appear independent of both  $z$  and roughness properties such that “tuning” model parameters is not necessary to predict stress transport in the roughness layer. However, roughness types spanning a wide range of statistical properties [73,74] including fragmented or “patchy” roughness [75,76] and porous surfaces such as gravel beds [77] are needed to confirm the invariance of the model parameters. We additionally note the present measurements do not include canopy roughness.

## V. DISCUSSION

The utility of structural models for  $\overline{u'w'w'}$  as closure of the turbulent shear stress budget is now discussed. The budget is simplified by first assuming  $M_{11} = \overline{u'w'}/\sigma_u\sigma_w$  is constant as earlier discussed. Using the first structural model from Eq. (13), the simplified momentum flux budget in Eq. (6) reduces to a linear first-order nonhomogeneous ordinary differential equation with variable

coefficients for the shear stress given as

$$A_1(z) \frac{d\overline{u'w'}}{dz} + \overline{u'w'} \left[ A_2(z) - \frac{C_R}{\tau(z)} \right] = (1 - C_I) \sigma_w^2 \frac{dU}{dz}, \quad (22)$$

where the last term on the right-hand side is the nonhomogeneous (or source) term (mechanical production in this case), and coefficients  $A_1(z)$  and  $A_2(z)$  are related to  $\Delta S_o$  as

$$\begin{aligned} A_1(z) &= \frac{2\sqrt{2\pi}}{\frac{1}{3}M_{11}(b_w - b_u) + (b_{uw} - 1)} \sigma_w \Delta S_o, \\ A_2(z) &= \frac{2\sqrt{2\pi}}{\frac{1}{3}M_{11}(b_w - b_u) + (b_{uw} - 1)} \frac{d(\sigma_w \Delta S_o)}{dz}. \end{aligned} \quad (23)$$

When  $A_1(z) \neq 0$ , the mathematical form of Eqs. (22) and (23) can then be compactly represented as

$$\begin{aligned} \frac{d\overline{u'w'}}{dz} + \overline{u'w'} P(z) &= Q(z), \\ P(z) &= \frac{1}{A_1(z)} \left[ A_2(z) - \frac{C_R}{\tau(z)} \right], \\ Q(z) &= \frac{1}{A_1(z)} \left[ (1 - C_I) \sigma_w^2 \frac{dU}{dz} \right]. \end{aligned} \quad (24)$$

The general solution can be derived using the integrating factor method  $\mu(z)$  to yield the shear stress at an arbitrary wall-normal position  $z = z_r$ :

$$\overline{u'w'}(z_r) \mu(z_r) = \overline{u'w'}(0) \mu(0) + \int_0^{z_r} Q(z) \mu(z) dz, \quad \mu(z) = \exp \left[ \int P(z) dz \right]. \quad (25)$$

The nonlocality of the relation between  $dU/dz$  and  $\overline{u'w'}$  is now evident. Specifically, to compute the turbulent stress at one arbitrary position  $z_r$  necessitates depth integration of  $Q(z)$  and  $P(z)$  from  $z = 0$  to  $z = z_r$ , and thus information on the turbulent state at other (i.e., nonlocal) positions. The determination of the precise shapes of  $Q(z)$  and  $P(z)$  necessitate knowledge of  $\sigma_w$ ,  $\tau(z)$ , and  $\Delta S_o$ , even when  $M_{11}$  is assumed to not vary appreciably with  $z$ . The focus here is on the shape of  $\Delta S_o$ , especially in the roughness sublayer, which is the least understood term in the list of variables impacting  $Q(z)$  and  $P(z)$ . Before discussing a possible generic shape for  $\Delta S_o$ , a number of points can be made. Equations (22) and (23) suggest that  $\overline{u'w'}$  is linearly related to  $dU/dz$  only when  $d(\overline{u'w'} \sigma_w \Delta S_o)/dz = 0$ . Otherwise, the connection between  $\overline{u'w'}$  and  $dU/dz$  is nonlocal. In contrast, K-theory predicts  $\overline{u'w'} = 0$  for  $dU/dz = 0$  as in Eq. (3). Returning to the  $\Delta S_o$  profile, its shape appears to be robust in canonical turbulent boundary layers as shown in Fig. 3, where the value  $\Delta S_o \approx -0.1$  is relatively constant within the log region. In the viscous buffer region,  $\Delta S_o$  changes sign consistently at  $z^+ \approx 15$  in both previous studies [3,8] and the present DNS case, suggesting the  $\Delta S_o(z^+)$  profile may be universal for the inner layer of smooth-wall flows.

While  $\sigma_w^+$  does not vary appreciably in the RSL, the behavior of  $\Delta S_o$  within the RSL is more difficult to parametrize. Figure 11 shows the  $\Delta S_o$  profile in the RSL, where position  $z$  is fixed relative to the top of the RSL,  $z_{\text{RSL}}$ . The position  $z_{\text{RSL}}$  was determined based on the start of the inertial dynamics, and the cylinder roughness cases are based on the third-order  $M_{ij}$  profiles as previously discussed. The increasing importance of sweep events due to roughness—reflected by  $\partial \Delta S_o / \partial z$ —is related closely with the roughness and canopy sublayer extent as suggested in the literature [9,15,21,78]. From Fig. 11, it is inconclusive as to whether the  $\Delta S_o$  profile is invariant in the upper portion of the RSL, or if the amplitude of  $\Delta S_o$  is a function of the roughness. Additional experiments are necessary to assess the sublayer trends in greater detail. A collapse of the curves within the RSL could not be achieved using a single roughness parameter such as  $k$  instead of the

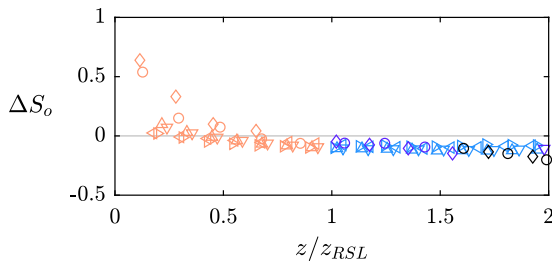


FIG. 11. Profiles of  $\Delta S_o$  in the sublayer of the rough-wall flow cases, where the position is relative to the RSL extent  $z_{RSL}$ . Data symbols correspond to the cases in Table I.

diagnostic parameter  $z_{RSL}$ . Similar to the extent of the RSL, it is likely that multiple roughness parameters, e.g., geometric roughness density in addition to height, are necessary to fully describe  $\Delta S_o$  [52]. Nonetheless, Fig. 11 establishes  $\Delta S_o$  as a function of the roughness and distance above the roughness in the RSL, demonstrating the relevance of the structural model in rough-wall flows as an alternative to neglecting transport entirely. While the present evidence does not provide a means to determine  $\Delta S_o$  *a priori* in the RSL, direct measurements of  $\Delta S_o$  can be used to predict stress transport through the structural model in Eq. (13). In short, the robust character of  $\Delta S_o$  can offer an extra closure constraint that may be exploited in Eq. (22), though a complete characterization of the  $\Delta S_o(z)$  profile is a topic better kept for a future inquiry. Such a characterization of  $\Delta S_o$ , in addition to general expressions for  $\sigma_w(z)$  and  $\tau(z)$ , is required to further advance the general solution in Eq. (25).

The present results can be used as a blue-print to inform wall modeling in large-eddy simulations or WRF. A common equilibrium wall model employed in simulations estimates the surface shear stress using the closest grid point and a log-law formulation based on the gradient diffusion relation in Eq. (3). It has been demonstrated here that this relation is insufficient if the first simulated point is within the RSL or CSL, in which case a correction for the stress transport is warranted. Further, Fig. 10 suggests the closure models for  $\overline{u'w'w'}$  based on  $\Delta S_o$  and  $\Gamma_+$  require less customization in the RSL than existing gradient-diffusion stress models using a mixing length. The derived structural models therefore provide a viable means to improve wall modeling within the sublayer. However, specific challenges must be addressed prior to practical implementation of the structural models in simulations. Foremost, the  $\Delta S_o$  profile shape and amplitude must be defined parametrically using  $k$  or  $k_s$  to characterize the RSL behavior and the transition to the inertial log layer. Figure 11 indicates such parametrization may be possible, at least for idealized “k-type” roughness geometries (i.e., roughness types where no recirculation exists within the spaces between the elements). The second challenge is to then solve for the stress, which is not straight forward as evidenced by the nonlocal connection between  $\Delta S_o$  and  $\overline{u'w'}$  in Eq. (25).

The key stated advantage of the  $\Delta S_o$  and  $\Gamma_+$  structural models is the possible universality in the model parameters, as opposed to the gradient-diffusion closure in Eq. (14) that requires tuning of the mixing length  $\ell_m(z)$  within the RSL. While not ideal, the assumed dependency  $\overline{u'w'w'} \propto \partial \overline{u'w'}/\partial z$  of the second-order gradient-diffusion closure may be deemed acceptable in Fig. 10(c) for specific applications. Specifically, second-order gradient diffusion accounts for the general trend of  $\overline{u'w'w'}(z)$ , despite error in the amplitude introduced by the choice of  $\ell_m$ . The result suggests that the connections explored here between surface roughness, velocity asymmetry, and the sweep/ejection imbalance can be further related to gradients in the second-order statistics. For instance, the CEM for  $\Delta S_o$  in Eq. (11) can be simplified using gradient-diffusion closures for the third-order moments rather than the linear relations employed earlier [22]. In this alternate simplification, there is a direct connection between the behavior of sweeps and ejections and gradients in the turbulent energy and shear stress.

## VI. CONCLUSIONS

When analyzing the momentum turbulent flux budget, it is shown that K-theory is valid where gradients in the transport term  $\partial \overline{u'w'w'}/\partial z$  are small relative to the production term. This condition is met in the logarithmic or equilibrium layer of the boundary layer, but transport is increasingly important within the viscous buffer and roughness sublayer regions. To provide a means for predicting stress transport in these regions, a link between the transport term  $\overline{u'w'w'}$  and asymmetry in the velocity statistics was established here using third-order cumulant expansion. One of the main assumptions in deriving this link is a proportionality between the third-order statistical moments  $M_{ij}$  that does not vary with roughness values (i.e.,  $b_{u,w,ww}$  are universal constants). The asymmetry manifests itself in a finite imbalance  $\Delta S_o$  between the contributions of sweeps and ejections to the momentum flux. The derived link between the turbulent flux transport term and  $\Delta S_o$  is shown to be analogous to other structural models representing the much studied transport of TKE ( $F_{\text{TKE}}$ ) near rough and smooth walls.

The coefficients  $b_{u,w,ww}$  in the derived structural model are shown here to be invariable with surface roughness for the limited number of roughness geometries tested, implying that the effect of roughness is entirely absorbed by  $\Delta S_o$ . The roughness effect can alternatively be quantified using a simpler metric of asymmetry  $\Gamma_+$  based on the fraction of time where  $u' > 0$ . The invariance of the model relations within the RSL also implies a form of “structural similarity” where the turbulent eddies maintain the same relations between  $\overline{u'w'w'}$ ,  $\Delta S_o$ ,  $\Gamma_+$ , and  $M_{ij}$  regardless of roughness and Reynolds number. The two structural models proposed have been compared against wind tunnel experiments and DNS for smooth and rough walls including two roughness geometries and one decade range in Reynolds number. The agreement between measured and modeled  $\overline{u'w'w'}$  is quite acceptable despite the numerous simplifications made.

While the structural model employing  $\Delta S_o$  was discussed here in more detail due to its physical implications, the diagnostic metric  $\Gamma_+$  is simpler to measure than  $\Delta S_o$  and the third-order moments  $M_{ij}$ . Thus, the second model may be convenient to employ in practice to assess the significance of the transport term. From a broader perspective, the link between  $\Gamma_+$  and the flux transport term may invite the use of telegraphic approximation and clustering properties in future work. Telegraphic approximation has received some attention in the boundary layer meteorology and turbulence literature [61,79–87] so as to establish analogies to concepts such as self-organized critically and intermittency. However, no connection to classical turbulence closure modeling has been offered. The work here may be viewed as an embryonic step in this direction.

## ACKNOWLEDGMENTS

The authors acknowledge funding support from the Institute on the Environment (IonE). Multiple authors are supported by the National Science Foundation: M.H. through a fellowship (NSF-AGS-2031312), M.G. through a CAREER Grant (No. NSF-CBET-1351303), and G.K. through Project Grants (No. NSF-AGS-1644382, No. NSF-IOS-1754893, and No. NSF-AGS-2028633). The authors are grateful to D. Squire, N. Hutchins, and co-authors for providing access to the sandpaper roughness data and to J. A. Sillero and co-authors for making the DNS database publicly available.

- 
- [1] B. J. Cantwell, Organized motion in turbulent flow, *Annu. Rev. Fluid Mech.* **13**, 457 (1981).
  - [2] S. K. Robinson, Coherent motions in the turbulent boundary layer, *Annu. Rev. Fluid Mech.* **23**, 601 (1991).
  - [3] J. M. Wallace, H. Eckelmann, and R. S. Brodkey, The wall region in turbulent shear flow, *J. Fluid Mech.* **54**, 39 (1972).
  - [4] W. W. Willmarth and S. S. Lu, Structure of the Reynolds stress near the wall, *J. Fluid Mech.* **55**, 65 (1972).

- [5] R. A. Antonia and J. D. Atkinson, High-order moments of Reynolds shear stress fluctuations in a turbulent boundary layer, *J. Fluid Mech.* **58**, 581 (1973).
- [6] S. S. Lu and W. W. Willmarth, Measurements of the structure of the Reynolds stress in a turbulent boundary layer, *J. Fluid Mech.* **60**, 481 (1973).
- [7] R. A. Antonia, Conditional sampling in turbulence measurement, *Annu. Rev. Fluid Mech.* **13**, 131 (1981).
- [8] H. Nakagawa and I. Nezu, Prediction of the contributions to the Reynolds stress from bursting events in open-channel flows, *J. Fluid Mech.* **80**, 99 (1977).
- [9] M. R. Raupach, Conditional statistics of Reynolds stress in rough-wall and smooth-wall turbulent boundary layers, *J. Fluid Mech.* **108**, 363 (1981).
- [10] P. J. A. Priyadarshana and J. C. Klewicki, Study of the motions contributing to the Reynolds stress in high and low Reynolds number turbulent boundary layers, *Phys. Fluids* **16**, 4586 (2004).
- [11] M. P. Schultz and K. A. Flack, The rough-wall turbulent boundary layer from the hydraulically smooth to the fully rough regime, *J. Fluid Mech.* **580**, 381 (2007).
- [12] G. G. Katul, G. Kuhn, J. Schieldge, and C.-I. Hsieh, The ejection-sweep character of scalar fluxes in the unstable surface layer, *Boundary-Layer Meteorol.* **83**, 1 (1997).
- [13] D. Li and E. Bou-Zeid, Coherent structures and the dissimilarity of turbulent transport of momentum and scalars in the unstable atmospheric surface layer, *Boundary-Layer Meteorol.* **140**, 243 (2011).
- [14] D. D. Baldocchi and T. P. Meyers, Turbulence structure in a deciduous forest, *Boundary-Layer Meteorol.* **43**, 345 (1988).
- [15] D. Poggi and G. G. Katul, The ejection-sweep cycle over bare and forested gentle hills: A laboratory experiment, *Boundary-Layer Meteorol.* **122**, 493 (2007).
- [16] C. Francone, G. G. Katul, C. Cassardo, and R. Richiardone, Turbulent transport efficiency and the ejection-sweep motion for momentum and heat on sloping terrain covered with vineyards, *Agr. Forest Meteorol.* **162**, 98 (2012).
- [17] J. J. Finnigan, Turbulence in waving wheat II. Structure of momentum transfer, *Boundary-Layer Meteorol.* **16**, 213 (1979).
- [18] T. Maitani and E. Ohtaki, Turbulent transport processes of momentum and sensible heat in the surface layer over a paddy field, *Boundary-Layer Meteorol.* **40**, 283 (1987).
- [19] R. H. Shaw, J. Tavangar, and D. P. Ward, Structure of the Reynolds stress in a canopy layer, *J. Climate Appl. Meteorol.* **22**, 1922 (1983).
- [20] H.-B. Su, R. H. Shaw, K. T. Paw, C.-H. Moeng, and P. P. Sullivan, Turbulent statistics of neutrally stratified flow within and above a sparse forest from large-eddy simulation and field observations, *Boundary-Layer Meteorol.* **88**, 363 (1998).
- [21] D. Poggi, A. Porporato, L. Ridolfi, J. D. Albertson, and G. G. Katul, The effect of vegetation density on canopy sublayer turbulence, *Boundary-Layer Meteorol.* **111**, 565 (2004).
- [22] D. Poggi, G. G. Katul, and J. D. Albertson, Momentum transfer and turbulent kinetic energy budgets within a dense model canopy, *Boundary-Layer Meteorol.* **111**, 589 (2004).
- [23] T. Watanabe, Large-eddy simulation of coherent turbulence structures associated with scalar ramps over plant canopies, *Boundary-Layer Meteorol.* **112**, 307 (2004).
- [24] D. Cava, G. G. Katul, A. Scrimieri, D. Poggi, A. Cescatti, and U. Giostra, Buoyancy and the sensible heat flux budget within dense canopies, *Boundary-Layer Meteorol.* **118**, 217 (2006).
- [25] C. Thomas and T. Foken, Flux contribution of coherent structures and its implications for the exchange of energy and matter in a tall spruce canopy, *Boundary-Layer Meteorol.* **123**, 317 (2007).
- [26] W. Yue, C. Meneveau, M. B. Parlange, W. Zhu, R. van Hout, and J. Katz, A comparative quadrant analysis of turbulence in a plant canopy, *Water Resour. Res.* **43**, W05422 (2007).
- [27] G. G. Katul, O. Peltola, T. Grönholm, S. Launiainen, I. Mammarella, and T. Vesala, Ejective and sweeping motions above a peatland and their role in relaxed-eddy-accumulation measurements and turbulent transport modelling, *Boundary-Layer Meteorol.* **169**, 163 (2018).
- [28] M. W. Rotach, Turbulence close to a rough urban surface part I: Reynolds stress, *Boundary-Layer Meteorol.* **65**, 1 (1993).
- [29] R. Moriwaki and M. Kanda, Local and global similarity in turbulent transfer of heat, water vapour, and CO<sub>2</sub>, *Boundary-Layer Meteorol.* **120**, 163 (2006).

- [30] L. Wang, D. Li, Z. Gao, T. Sun, X. Guo, and E. Bou-Zeid, Turbulent transport of momentum and scalars above an urban canopy, *Boundary-Layer Meteorol.* **150**, 485 (2014).
- [31] J. C. Wyngaard and C.-H. Moeng, Parameterizing turbulent diffusion through the joint probability density, *Boundary-Layer Meteorol.* **60**, 1 (1992).
- [32] K. Ghannam, T. Duman, S. T. Salesky, M. Chamecki, and G. G. Katul, The non-local character of turbulence asymmetry in the convective atmospheric boundary layer, *Q. J. R. Meteorol. Soc.* **143**, 494 (2017).
- [33] S. T. Salesky, M. Chamecki, and E. Bou-Zeid, On the nature of the transition between roll and cellular organization in the convective boundary layer, *Boundary-Layer Meteorol.* **163**, 41 (2017).
- [34] G. D. Katsouvas, C. G. Helmis, and Q. Wang, Quadrant analysis of the scalar and momentum fluxes in the stable marine atmospheric surface layer, *Boundary-Layer Meteorol.* **124**, 335 (2007).
- [35] E. A. Variano and E. A. Cowen, Turbulent transport of a high-Schmidt-number scalar near an air–water interface, *J. Fluid Mech.* **731**, 259 (2013).
- [36] I. Fer, M. G. McPhee, and A. Sirevaag, Conditional statistics of the Reynolds stress in the under-ice boundary layer, *Geophys. Res. Lett.* **31**, L15311 (2004).
- [37] J. M. Wallace, Quadrant analysis in turbulence research: History and evolution, *Annu. Rev. Fluid Mech.* **48**, 131 (2016).
- [38] I. Marusic, B. J. McKeon, P. A. Monkewitz, H. M. Nagib, A. J. Smits, and K. R. Sreenivasan, Wall-bounded turbulent flows at high Reynolds number: Recent advances and key issues, *Phys. Fluids* **22**, 065103 (2010).
- [39] A. J. Grass, Structural features of turbulent flow over smooth and rough boundaries, *J. Fluid Mech.* **50**, 233 (1971).
- [40] P. Å. Krogstad, R. A. Antonia, and L. W. B. Browne, Comparison between rough- and smooth-wall turbulent boundary layers, *J. Fluid Mech.* **245**, 599 (1992).
- [41] K. A. Flack, M. P. Schultz, and T. A. Shapiro, Experimental support for Townsend’s Reynolds number similarity hypothesis on rough walls, *Phys. Fluids* **17**, 035102 (2005).
- [42] A. A. Townsend, Equilibrium layers and wall turbulence, *J. Fluid Mech.* **11**, 97 (1961).
- [43] F. N. Frenkiel and P. S. Klebanoff, Higher-order correlations in a turbulent field, *Phys. Fluids* **10**, 507 (1967).
- [44] F. N. Frenkiel and P. S. Klebanoff, Probability distributions and correlations in a turbulent boundary layer, *Phys. Fluids* **16**, 725 (1973).
- [45] B. E. Launder, G. J. Reece, and W. Rodi, Progress in the development of a Reynolds-stress turbulence closure, *J. Fluid Mech.* **68**, 537 (1975).
- [46] G. L. Mellor and T. Yamada, Development of a turbulence closure model for geophysical fluid problems, *Rev. Geophys.* **20**, 851 (1982).
- [47] G. G. Katul and J. Albertson, An investigation of higher-order closure models for a forested canopy, *Boundary-Layer Meteorol.* **89**, 47 (1998).
- [48] Y. Nagano and M. Tagawa, A structural turbulence model for triple products of velocity and scalar, *J. Fluid Mech.* **215**, 639 (1990).
- [49] J. J. Finnigan, Turbulence in plant canopies, *Annu. Rev. Fluid Mech.* **32**, 519 (2000).
- [50] G. G. Katul, A. Porporato, C. Manes, and C. Meneveau, Co-spectrum and mean velocity in turbulent boundary layers, *Phys. Fluids* **25**, 091702 (2013).
- [51] M. R. Raupach and A. S. Thom, Turbulence in and above plant canopies, *Annu. Rev. Fluid Mech.* **13**, 97 (1981).
- [52] M. R. Raupach, R. A. Antonia, and S. Rajagopalan, Rough-wall turbulent boundary layers, *Appl. Mech. Rev.* **44**, 1 (1991).
- [53] S. B. Pope, *Turbulent Flows* (Cambridge University Press, Cambridge, 2000).
- [54] L. Prandtl, Bericht über Untersuchungen zur ausgebildeten Turbulenz, *ZAMM (Z. Angew. Math. Mech.)* **5**, 136 (1925).
- [55] M. Heisel, T. Dasari, Y. Liu, J. Hong, F. Coletti, and M. Guala, The spatial structure of the logarithmic region in very-high-Reynolds-number rough wall turbulent boundary layers, *J. Fluid Mech.* **857**, 704 (2018).



- [56] M. Heisel, C. M. de Silva, N. Hutchins, I. Marusic, and M. Guala, On the mixing length eddies and logarithmic mean velocity profile in wall turbulence, *J. Fluid Mech.* **887**, R1 (2020).
- [57] S. Corrsin, Limitations of gradient transport models in random walks and in turbulence, *Adv. Geophys.* **18**, 25 (1975).
- [58] J. W. Deardorff, Closure of second-and third-moment rate equations for diffusion in homogeneous turbulence, *Phys. Fluids* **21**, 525 (1978).
- [59] G. G. Katul, C.-I. Hsieh, G. Kuhn, D. Ellsworth, and D. Nie, Turbulent eddy motion at the forest-atmosphere interface, *J. Geophys. Res.* **102**, 13409 (1997).
- [60] G. G. Katul, D. Poggi, D. Cava, and J. J. Finnigan, The relative importance of ejections and sweeps to momentum transfer in the atmospheric boundary layer, *Boundary-Layer Meteorol.* **120**, 367 (2006).
- [61] D. Cava, G. G. Katul, A. Molini, and C. Elefante, The role of surface characteristics on intermittency and zero-crossing properties of atmospheric turbulence, *J. Geophys. Res.* **117**, D01104 (2012).
- [62] J. A. Sillero, J. Jiménez, and R. D. Moser, One-point statistics for turbulent wall-bounded flows at Reynolds numbers up to  $\delta^+ \approx 2000$ , *Phys. Fluids* **25**, 105102 (2013).
- [63] M. R. Raupach, A. S. Thom, and I. Edwards, A wind tunnel study of turbulent flow close to regularly arrayed rough surfaces, *Boundary-Layer Meteorol.* **18**, 373 (1980).
- [64] D. T. Squire, C. Morrill-Winter, N. Hutchins, I. Marusic, M. P. Schultz, and J. C. Klewicki, Smooth- and rough-wall boundary layer structure from high spatial range particle image velocimetry, *Phys. Rev. Fluids* **1**, 064402 (2016).
- [65] D. T. Squire, C. Morrill-Winter, N. Hutchins, M. P. Schultz, J. C. Klewicki, and I. Marusic, Comparison of turbulent boundary layers over smooth and rough surfaces up to high Reynolds numbers, *J. Fluid Mech.* **795**, 210 (2016).
- [66] T. Wei, P. Fife, J. C. Klewicki, and P. McMurtry, Properties of the mean momentum balance in turbulent boundary layer, pipe and channel flows, *J. Fluid Mech.* **522**, 303 (2005).
- [67] K. Chauhan, J. Philip, C. M. de Silva, N. Hutchins, and I. Marusic, The turbulent/non-turbulent interface and entrainment in a boundary layer, *J. Fluid Mech.* **742**, 119 (2014).
- [68] J. Jiménez, Turbulent flows over rough walls, *Annu. Rev. Fluid Mech.* **36**, 173 (2004).
- [69] A. A. Townsend, *The Structure of Turbulent Shear Flow*, 2nd ed. (Cambridge University Press, Cambridge, 1976).
- [70] J. C. Kaimal and J. J. Finnigan, *Atmospheric Boundary Layer Flows* (Oxford University Press, New York, 1994).
- [71] L. H. Benedict and R. D. Gould, Towards better uncertainty estimates for turbulence statistics, *Exp. Fluids* **22**, 129 (1996).
- [72] B. N. Bailey and R. Stoll, The creation and evolution of coherent structures in plant canopy flows and their role in turbulent transport, *J. Fluid Mech.* **789**, 425 (2016).
- [73] A. Busse, M. Thakkar, and N. D. Sandham, Reynolds-number dependence of the near-wall flow over irregular rough surfaces, *J. Fluid Mech.* **810**, 196 (2017).
- [74] J. M. Barros, M. P. Schultz, and K. A. Flack, Measurements of skin-friction of systematically generated surface roughness, *Int. J. Heat Fluid Fl.* **72**, 1 (2018).
- [75] S. Dupont and Y. Brunet, Coherent structures in canopy edge flow: A large-eddy simulation study, *J. Fluid Mech.* **630**, 93 (2009).
- [76] C. Poëtte, B. Gardiner, S. Dupont, I. Harman, M. Böhm, J. J. Finnigan, D. Hughes, and Y. Brunet, The impact of landscape fragmentation on atmospheric flow: A wind-tunnel study, *Boundary-Layer Meteorol.* **163**, 393 (2017).
- [77] C. Manes, D. Poggi, and L. Ridolfi, Turbulent boundary layers over permeable walls: Scaling and near-wall structure, *J. Fluid Mech.* **687**, 141 (2011).
- [78] S. C. Gleicher, M. Chamecki, S. A. Isard, Y. Pan, and G. G. Katul, Interpreting three-dimensional spore concentration measurements and escape fraction in a crop canopy using a coupled Eulerian–Lagrangian stochastic model, *Agr. Forest Meteorol.* **194**, 118 (2014).
- [79] A. Bershadskii, J. J. Niemela, A. Praskovsky, and K. R. Sreenivasan, “Clusterization” and intermittency of temperature fluctuations in turbulent convection, *Phys. Rev. E* **69**, 056314 (2004).

- [80] D. Cava and G. G. Katul, The effects of thermal stratification on clustering properties of canopy turbulence, *Boundary-Layer Meteorol.* **130**, 307 (2009).
- [81] D. Cava, L. Mortarini, U. Giostra, O. Acevedo, and G. G. Katul, Submeso motions and intermittent turbulence across a nocturnal low-level jet: A self-organized criticality analogy, *Boundary-Layer Meteorol.* **172**, 17 (2019).
- [82] Q. Li and Z. Fu, The effects of non-stationarity on the clustering properties of the boundary-layer vertical wind velocity, *Boundary-Layer Meteorol.* **149**, 219 (2013).
- [83] J. L. Lumley, Some comments on turbulence, *Phys. Fluids A* **4**, 203 (1992).
- [84] D. Poggi and G. G. Katul, Evaluation of the turbulent kinetic energy dissipation rate inside canopies by zero-and level-crossing density methods, *Boundary-Layer Meteorol.* **136**, 219 (2010).
- [85] D. Poggi and G. G. Katul, Flume experiments on intermittency and zero-crossing properties of canopy turbulence, *Phys. Fluids* **21**, 065103 (2009).
- [86] K. R. Sreenivasan and A. Bershadskii, Clustering properties in turbulent signals, *J. Stat. Phys.* **125**, 1141 (2006).
- [87] K. R. Sreenivasan and A. Bershadskii, Finite-Reynolds-number effects in turbulence using logarithmic expansions, *J. Fluid Mech.* **554**, 477 (2006).